Magnetic Tunability of Permalloy Artificial Spin Ice Structures

A. Talapatra,[1] N. Singh,[2] and A. O. Adeyeye[1,*,†]

[1]*Information Storage Materials Laboratory, Department of Electrical and Computer Engineering, National University of Singapore, 117576, Singapore*

[2]*Institute of Microelectronics, A*STAR, 2, Fusionopolis Way, 138634, Singapore*

This paper reports tunable $Ni_{80}Fe_{20}$ artificial spin ice structures of various geometrical lattice arrangements as a function of film thickness. We achieve the magnetic tunability by three distinct methods namely, geometrical arrangements of nanomagnetic elements in the form of square, kagome, and triangular lattices with the variation in film thickness (20, 30, and 50 nm) for each geometry and the applied field orientations. Magnetic force microscopy reveals that the nanoelements are in single-domain states, obeying the spin ice rules for the 20-nm-thick spin ice structures. A combination of nanoelements in single-domain and vortex states is observed with the increase in thickness up to 30 nm. For the 50-nm-thick elements, vortex and flux closure states are in evidence. Broadband ferromagnetic resonance spectroscopy establishes the presence of distinct resonant modes that are spatially localized in the nanomagnets of different orientations and, hence, can be controlled by the applied field orientations. The role of shape anisotropy on the static and dynamic properties is investigated systematically and complemented by extensive micromagnetic simulations. The results show great potential towards designing reconfigurable magnonic crystals for microwave filter applications.

I. INTRODUCTION

Magnetic nanostructures are the building blocks for a number of spintronic technologies including spin-valve-based devices [1], high-density patterned media [2] to scalable magnetic skyrmions [3,4] for next-generation ultra-high-density storage. Unlike continuous thin film media, arrays of magnetic nanostructures introduce magnetostatic interaction between the neighboring islands, which modifies the collective switching process and broadens the switching field distribution [5,6]. The modification of static and dynamic magnetic properties as a function of size, shape, and distribution of magnetic dots [7–9] and antidots [10–12] has been studied extensively where the importance of configurational anisotropy was explained. Unlike dots with spherical symmetry, the structures with large aspect ratios such as nanowire (NW) can introduce shape anisotropy and, hence, play a significant role in engineering magnetic properties [13–15]. In addition, periodic width modulations in coupled NWs can act as reconfigurable magnonic crystals with spatial localization of magnon modes [16–18]. The magnetic properties of the NWs can further be modified by creating NW assemblies of different structural symmetry,

which are the building blocks for artificial spin ice (ASI) [19,20]. ASI structures, consisting of arrays of interacting, single-domain nanomagnets (NMs) are promising model systems to explore microscopic features of geometrical frustration, which leads to the magnetic states with strong correlations and local ordering. Specific geometries having higher symmetry with repeatable unit cells result in degeneracy in the ground states, which is exploited as the frustrated state of the system [21]. Owing to its equivalence to the electrical charge distribution, each component of ASI can be considered as a magnetic dipole with a positive and negative charge $(\pm q)$ separated by one lattice spacing. Thus, the ice rule can be described in terms of local minimization of magnetic charges at each lattice site.

The trend towards creating geometrical frustration in nanomagnetic systems has been a topic of intense research in the last few years. The literature reports geometrically frustrated ASI structures with the shape of square spin ice (SSI) [22], kagome spin ice (KSI) [23], shakti lattice [24], tetris lattice [25], and coupled islands [26]. The field-induced phase coexistence [26], topologically protected kinetics and charge transfer [24], frustration-induced reduction of dimensionality [25] have been discussed for different geometries. The unique geometry of individual structure leads to the various ground state magnetic charge configurations with different degeneracies. As a result, most of the research attempts highlight the

---

*[*]eleaao@nus.edu.sg

[†]Present affiliation: Department of Physics, Durham University, South Rd, Durham, DH1 3LE, UK

manipulation of the degeneracy of magnetic ground state and observation of magnetic monopoles with the analysis of spin mapping and correlation of spins at different vertex using magnetic force microscopy (MFM) [22,27], x-ray magnetic circular dichroism (XMCD) photoemission electron microscopy (PEEM) [28–30], and Lorentz microscopy [31]. Apart from the static magnetic properties of ASI, tunability in magnetization dynamics by breaking the angular symmetry of the structure [32] and geometry-dependent existence of magnon modes [33,34] have been reported. Recently, the tenability of the ice rules, ground state degeneracy has also been reported for aperiodic structures [35], pinwheel structures [36], and colloidal systems [37].

In this paper, we conduct a detailed comparative study on the variation of magnetic properties (static and dynamic) of ASI of Permalloy (Py) $Ni_{80}Fe_{20}$ with different geometries and thicknesses (d). Although Py is a well-investigated ferromagnetic system, the advantages of studying nanostructures with Py include high-volume magnetization to ensure strong interaction between the neighboring islands. Second, the Curie temperature of bulk Py is relatively high enough to make the system magnetically stable at room temperature. Most importantly, Py offers effectively zero magnetocrystalline anisotropy, which results in the dominance of the geometry of the system and, hence, the shape anisotropy plays the key role in determining the magnetization reversal mechanism. While the structural geometry is responsible for tuning the shape anisotropy or the configurational anisotropy of the system, the strength of dipolar coupling is modified by the film thickness. The previous work by Zhou *et al*. on a Py ASI system [38] was limited to the investigation of the static and dynamic behavior at a relatively low magnetic field for 25-nm-thick spin ice and anti-spin ice structures. In the present work, we investigate the effects of film thickness on the evolution of complex spin texture in ASI structures beyond the single-domain state that has been discussed in the literature so far. We conduct a comparative study of the magnetization reversal processes and associated dynamic behavior at high field of ASI geometries such as SSI, KSI, and comparatively newer triangular spin ice (TSI) structures [39]. This comparative study shows a deep insight towards the realization of ice rules at lower thicknesses and the critical thickness for the decomposition of single-domain states to hybrid spin states along with its implication on magnetization dynamics for the ASI structures. The results on magnetization dynamics explain the dependence of various spin wave modes and their spatial localization on the structural symmetry, film thickness, and applied field (H_{app}) orientation. The experimental observations of static and dynamic magnetic behavior have been complemented by micromagnetic simulations, using the OOMMF package [40]. There is good agreement between the experimental results and micromagnetic simulations.

II. FABRICATION AND EXPERIMENTAL DETAIL

The 2D ASI structures are patterned over a large area of 4×4 mm^2 using deep ultraviolet (DUV) lithography at an exposure wavelength of 193 nm to define the pattern of the corresponding structures in a 240-nm-thick layer of resist on top of a 60-nm-thick bottom antireflection coating on Si substrates. Detailed processes related to DUV lithography, adapted for this work, are described in Ref. [41]. The lithographic process is followed by the electron beam deposition of Py films of various thicknesses, in the range from 20 to 50 nm on top of a Cr (5 nm) adhesive layer, in a chamber, with a base pressure less than 5×10^{-8} Torr and the deposition rate is maintained at 0.2 Å/s. Thereafter, the samples are soaked in a DUV resist removal solution (OK 73 resist thinner) for 1 h, followed by lift-off in an ultrasonic bath.

A field-emission-gun scanning electron microscope (SEM) is used to verify the completion of the lift-off process and to inspect the quality of the fabricated nanostructures. The collective magnetization reversal process is investigated using superconducting quantum interference device (SQUID) with applied magnetic field angles (ϕ) at 0° and 45°. Magnetic force microscopy (MFM) with CoCr-coated n-type Si tips is used to directly map the magnetization ground states of the samples at remanence. Before the MFM imaging, the samples are saturated with H_{app} of 10 kOe and, thereafter, the field is brought back to zero to confirm the remanent states. The dynamic responses are characterized using two different ferromagnetic resonance (FMR) setups at room temperature. The 20-nm-thick Py ASI structures are studied by employing broadband FMR with a vector network analyzer (VNA) in the frequency range from 50 MHz to 20 GHz where a ground-signal-ground (G-S-G) type of coplanar waveguide is used to pass the radiofrequency current, generating the excitation field h_{rf}, mutually perpendicular to H_{app}, generated by a rotatable projection magnet with maximum field range of ± 1.4 kOe. For this approach, the frequency is varied at a constant field. In order to characterize the thicker samples, another FMR setup with magnetic field sweep of ± 4.5 kOe is used at constant frequency (f). Here, the samples are placed on top of stripline and VNA is used to generate the h_{rf} with lock-in detection of the derivative of the absorbed power (dP/dH). Depending on the region of interest, the frequency range of h_{rf} is chosen within 10–16 GHz.

III. RESULTS AND DISCUSSIONS

The representative SEM images of the fabricated arrays of nanostructures are shown in Fig. 1(a), depicting the SSI, KSI, and TSI lattice arrangements. The SEM images confirm a good lift-off for the resist and depict uniformity of the nanostructures over a large area. The dimension of the individual magnetic elements constituting each lattice
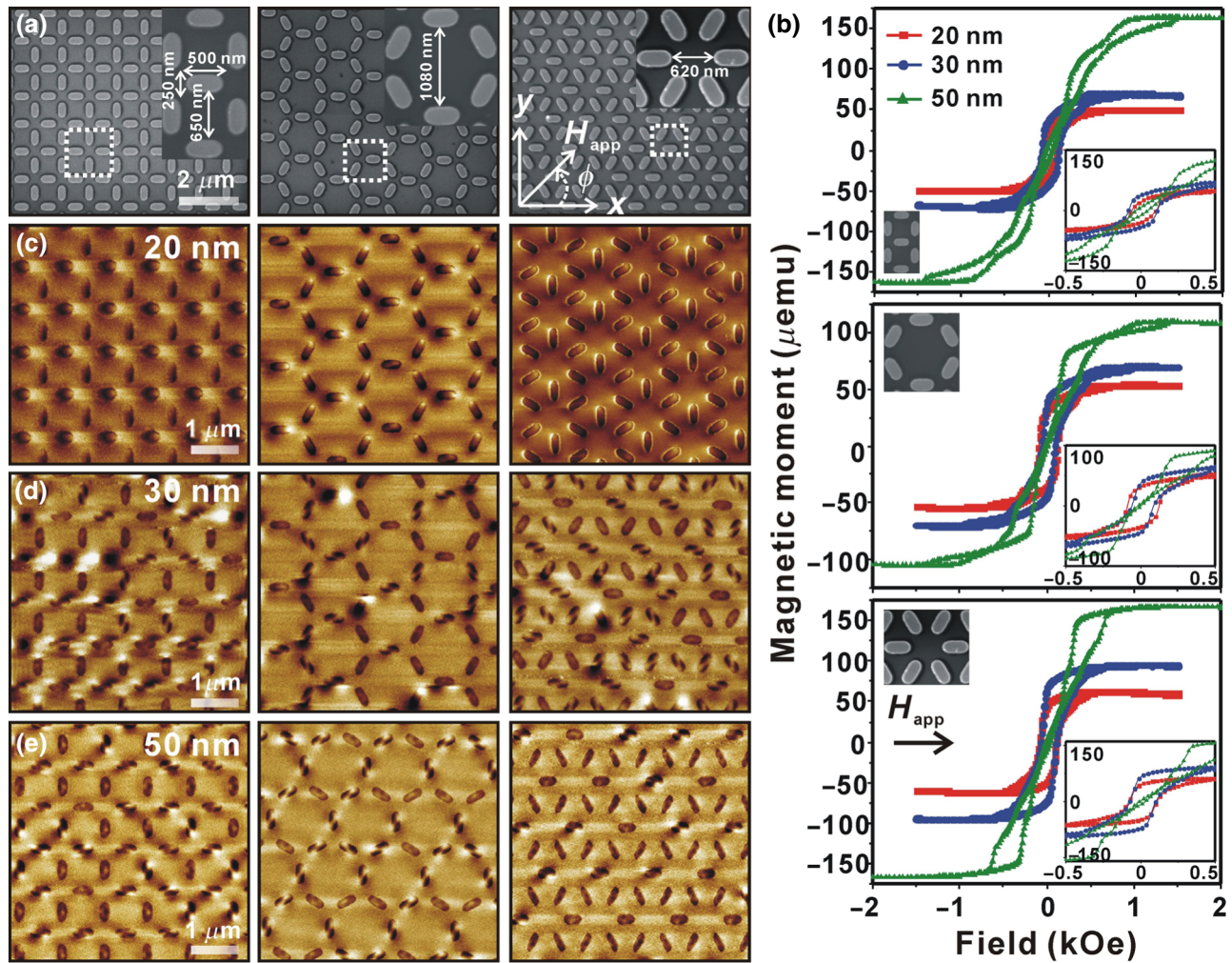
FIG. 1. (a) SEM images of the Py nanomagnets arranged in different ASI lattices, SSI, KSI, and TSI, respectively, from left to right with magnified view as insets, describing the dimensions (the white dotted box represents a single repetitive unit for the entire geometry), (b) corresponding hysteresis loops ($\phi = 0°$) for the different spin ice structures (shown as left insets) for $d = 20$, 30, and 50 nm with magnified views (right insets) in the field range of ± 0.5 kOe. MFM images of the different spin ice lattice arrangements at remanence for ASI structures of thicknesses (c) 20 nm, (d) 30 nm, and (e) 50 nm.

arrangement is of length (l) = 500 nm, width (w) = 250 nm with an aspect ratio of 2:1, similar for all the samples. Based on our initial micromagnetic simulations, the choice of dimensions of the nanoelements ensures that Landau patterns are easily accessible in the individual nanoelements within the thickness range investigated. Other geometrical details are indicated in the insets of Fig. 1(a). For the SSI, the neighboring islands are perpendicular to each other and four islands meet at one vertex (marked by the dotted box), whereas for KSI, each neighboring lattice makes an angle of 120° with each other (shown inside the dotted box). In the TSI geometry, each vertex is made of six nanomagnets at different orientations and the entire geometry can be expressed as periodic repetitions of equilateral triangles, as marked by the dotted box in Fig. 1(a). Thus, the configurational anisotropy is created by two

mutually perpendicular NMs for SSI and three neighboring NMs for each of KSI and TSI. Owing to the change in geometry of the respective components, the magnetostatic interactions between the NMs for KSI and TSI are also different. For SSI, the number of possible ground state configurations are 16 (2^4), distributed in 4 different topologies whereas KSI displays 8 (2^3) configurations in 2 different topologies [21] and TSI contains 64 (2^6) configurations distributed in 8 topologies [39].

A. Magnetization reversal processes

The hysteresis loops for the different ASI lattice configurations are shown in Fig. 1(b) for $d = 20$, 30, and 50 nm. The magnetization reversal process and detail features of the hysteresis loops are markedly sensitive to the lattice

TABLE I.   The values of H_c and squareness of the ASI structures as a function of thickness and geometry.

Thickness (nm)	H_c (Oe)			Squareness (%)		
	SSI	KSI	TSI	SSI	KSI	TSI
20	82	105	93	51.6	61.5	74.2
30	95	73	87	55.1	57.1	72
50	39	9	20	6.1	2	3.2

arrangements and film thickness. The magnetic moments of the samples clearly scale with the film thickness. The net moment is observed to be highest for the TSI structure, followed by SSI and KSI as the geometric arrangements allow the maximum number density of NMs for TSI and minimum for the KSI structure, which can be seen from Fig. 1(a). The values of coercive field (H_c) and squareness (ratio of remanent to saturation magnetization) are listed in Table I for comparison. The distinct thickness-dependent reversal processes result in smaller H_c values for the 50-nm-thick ASI structures in comparison with those for the 20- and 30-nm-thick ASI structures, irrespective of their geometry. Figure 1(b) shows a single-step switching of magnetization for the thinner ASI structures whereas the 50-nm-thick structures depict slanted hysteresis loops with multiple steps. For 50-nm-thick SSI, the first and second switching steps are observed around 950 and 270 Oe after which a decrease in magnetization leads to the reverse saturated configuration. For KSI and TSI, the sharp decrease of magnetization takes place around 230 and 360 Oe, respectively. The squareness values of these loops are close to zero, in contrast to the thinner films, as recorded in Table I. The intriguing reversal phenomena are the driving force behind the understanding of the spin configurations of the ASI structures of different thicknesses. MFM is performed to directly image the magnetic ground state at zero field (remanent state). Shown in Fig. 1(c) are the MFM images for $d = 20$ nm and $\phi = 0°$ for all the lattice arrangements of ASI structures. The MFM images clearly indicate that the magnetic elements are in single-domain states with dark and bright spots indicating the positive and negative saturation, respectively, for $\phi = 0°$ for all the lattice arrangements of ASI. The magnetization in most of the vertices obeys the ice rule, "two-in two-out" for SSI, and "one-in two-out" or "two-in one-out" for KSI. Interestingly, the single-domain spin configuration for few of the NMs breaks into vortex of different chirality at $d = 30$ nm, clearly observed from Fig. 1(d). Thus, the 30-nm-thick ASI structures display the evolution of single-domain and vortex spin configurations at remanence. In addition to the lattice arrangements of the ASI, film thickness also plays an important role in controlling the dipolar coupling between the elements. Shown in Fig. 1(e) are the MFM images for $d = 50$ nm and $\phi = 0°$ for all the lattice arrangements of ASI structures. The magnetic

elements constituting the ASI are in the vortex state of different (random) chiralities for all the structures. Owing to the smaller core diameter, the polarities of the vortex cores cannot be properly identified from the MFM images. For a fixed scanned area, the density of vortex states is strongly dependent on the lattice arrangements and film thickness. The single-domain magnetic islands are no longer observed, instead, the magnetic elements with comparatively lower contrast (other than the vortex state), probably display flux closure configurations. The linear decrease of magnetization and negligible remanence for 50-nm-thick ASI structures [as shown in Fig. 1(b)] may be attributed to the formation of vortex and flux closure configurations, which lowers the magnetic energy of the system by reducing the stray fields and, hence, minimizing the magnetostatic energy of the system [42]. The chirality, position of the vortex, and polarity of the vortex cores are modified with the application of magnetic field [43,44]. Thus, increasing the magnetic field towards saturation results in the deformation of the vortex by moving its core away from the center of the nanomagnet, until it becomes unstable and, finally, the vortex is annihilated [45]. From the previous discussion, it is very clear that the magnetization reversal for the 50-nm-thick nanostructures is essentially dominated by the nucleation, displacement, and annihilation of the vortex core. The observed differences in the magnetization states at remanence for the three film thicknesses are expected because the ground state of magnetization is the manifestation of the minimized total free energy (F) of the system. This can be expressed as

$$F = \iiint E \, dv \tag{1}$$

representing the volume integral of the energy density (E), consisting of magnetocrystalline anisotropy, exchange energy, magnetostatic energy, and Zeeman energy. The formation of magnetic domains is due to the change in magnetization (**M**) orientation, which is defined as

$$\frac{\partial \mathbf{M}(\mathbf{r},\, t)}{\partial t} = -L\,\frac{\delta F}{\delta \mathbf{M}(\mathbf{r},\, t)} \tag{2}$$

where **r** is the position vector at which **M** is calculated at a particular time t and L is the kinetic coefficient. Hence, Eqs. (1) and (2) essentially bridge the relationship between the role of net magnetic energy and ground state magnetization of a system. Thus, the correlation between Fig. 1(b) and Figs. 1(c)–1(e) clearly explains the static magnetic properties along with the magnetization reversal mechanism of the different lattice arrangements of ASI. The hysteresis loops retain similar features with an enhancement of H_c for $\phi = 45°$, which is in agreement with the literature [46]. The vortex states are visible with modified vortex density for $d = 50$ nm. The hysteresis loops and

MFM images for 50-nm-thick ASI structures with $\phi = 45°$ are shown in Fig. S1 of the Supplemental Material [47].

B. Magnetization dynamics

Shown in Fig. 2(a) are the representative FMR spec-

tra for 20-nm-thick ASI nanostructures at saturated states with $H_{app} = -1.4$ kOe for $\phi = 0°$ and $45°$. Two distinct resonance peaks exist for all the ASI structures for $\phi = 0°$. If we consider the shape anisotropy of individual NM, the FMR spectra can be explained using the Kittel equation [48],

$$\omega = \gamma \sqrt{\{[H_{app} + (N_z - N_H)4\pi M_s] \times [H_{app} + (N_{H\perp} - N_H)4\pi M_s]\}}$$ (3)

where N_H and $N_{H\perp}$ are the demagnetizing factors for the nanostructure along H_{app} and mutually perpendicular to H_{app}, respectively, N_z is the demagnetizing factor along the thickness of the film, γ is the gyromagnetic ratio, and $4\pi M_s$ is the magnetization of the sample at -1.4 kOe.

For $\phi = 0°$ and SSI in Fig. 2(a), $N_{H\perp}$ is larger than N_H for the horizontal NMs as H_{app} is applied along their easy axis. For the vertically arranged NMs, the situation is reversed. Hence, two resonance peaks are observed at 9.9 GHz (a_1) and 12.1 GHz (a_2), which corresponds to the

modes localized in the vertical and horizontal nanomagnets, respectively. As the SSI geometry offers the number density of the horizontal and vertical NMs nearly equal within the signal line of the coplanar waveguide, the intensities of both the resonance peaks become comparable. Interestingly, the FMR spectra for $\phi = 45°$ is significantly modified showing a single resonance peak at 10.9 GHz (a'_1) for SSI. As the nanomagnets are arranged in mutually perpendicular orientation for SSI, so the SSI system has a structural symmetry along $45°$, resulting in identical in-plane demagnetization factors for both the horizontal and vertical NMs. Hence, the single resonance mode at a'_1 should be localized in all the NMs, irrespective of their orientations.

For KSI in Fig. 2(a), the resonance modes appear at 9.3 GHz (b_1) and 11.7 GHz (b_2) for $\phi = 0°$. In this arrangement, only the horizontal NMs are colinear with the easy axis whereas the tilted NMs make an angle of $60°$ with respect to the easy axis. Hence, $N_{H\perp}$ is smaller for the tilted NMs compared with that for the horizontal NMs. This results in the presence of two distinct modes, localized in the horizontal NMs and all the tilted NMs. On the other hand, for $\phi = 45°$, all three NMs (in a single repetitive unit) become tilted at three different orientations with respect to H_{app}. Thus, three distinct resonance peaks appear at 9.2 GHz (b'_1), 10.9 GHz (b'_2) and 12.1 GHz (b'_3) for KSI at $\phi = 45°$. According to the geometry, indicated in Fig. 1(a), b'_2 should be localized in the horizontal NMs with b'_1 and b'_3 localized in the NMs tilted at larger and smaller angles, respectively, with respect to H_{app}.

The dynamic response of TSI has a similarity with that of KSI, as shown in Fig. 2(a). This is expected because TSI also contains a repetitive arrangement of three nanomagnets arranged in a triangular lattice [Fig. 1(a)]. For $\phi = 0°$, H_{app} is applied along the easy axis for the horizontal NMs, experiencing smaller N_H compared with the tilted NMs. Hence, two resonance modes are observed in which the mode at 12.1 GHz (c_2) is localized in the horizontal NMs and the mode at 10.3 GHz (c_1) is localized in all the tilted NMs. Similar to the KSI arrangement, three
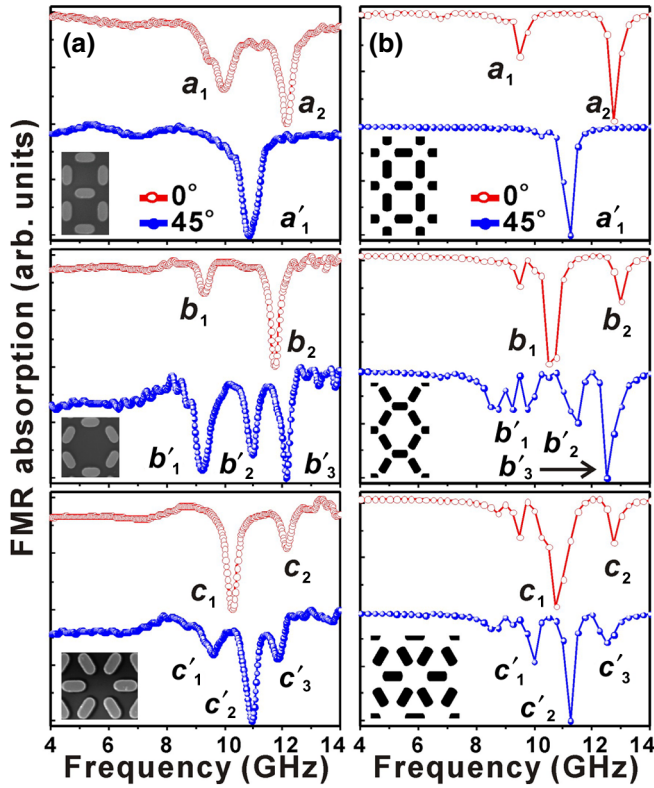

FIG. 2. (a) Experimental and (b) simulated FMR spectra (at $H_{app} = -1.4$ kOe) for 20-nm-thick Py spin ice (structures are depicted as insets).

distinct peaks are observed at 9.6 GHz (c'_1), 10.9 GHz (c'_2), and 11.8 GHz (c'_3) for TSI at $\phi = 45°$. Following the same reason as mentioned previously, the mode c'_2 should be localized in the horizontal NMs. Unlike SSI, we have observed an asymmetry in peak intensity for KSI and TSI at $\phi = 0°$ [Fig. 2(a)]. The number density of the tilted NMs is higher compared with the horizontal NMs and, hence, the mode localized in the tilted NMs is expected to be higher in intensity. The experimental results are in good agreement with the previously reported results [38].

In order to further understand the experimental results shown in Figs. 2(a), 3D micromagnetic simulation is performed as shown in Fig. 2(b). The standard parameters for Py are used as the input parameters, include exchange constant $A = 1.3 \times 10^{-6}$ erg cm^{-1}, saturation magnetization $M_s = 800$ emu.cm^{-3} with zero uniaxial anisotropy (K_u). The damping constant (α) of bulk Py used is 0.008 with γ as 2.8 GHz kOe^{-1}. The masks used in the simulations are derived from the SEM images and consist of one-unit cell with the provision for applying 2D periodic boundary conditions along l and w directions [shown as the insets of Fig. 2(b)] to avoid the effect of confinement. Cuboidal cells of volume $5 \times 5 \times 10$ nm^3 are used in the simulations. Initializing with a randomly magnetized state, the system can relax following the Landau-Lifshitz-Gilbert (LLG) equation [49] with a stopping criterion of $d\mathbf{M}/dt = 0.1$ deg/ns. After achieving the ground state, the sample is saturated along the x axis and then hysteresis loops are measured by sweeping the field. The simulated hysteresis loops have been depicted in Fig. S2 of the Supplemental Material [47], which qualitatively agrees with the experimental results of Fig. 1(b). For the dynamic simulations, the magnetization state at the field of interest (in this case −1.4 kOe) is recorded and used as the input. In order to calculate the dynamic response, a sinc pulse of amplitude 50 Oe is applied along the z direction to perturb the magnetization of the system. The variation of magnetization is recorded for 4 ns within which it completely damps out. The sampling interval is fixed at 10 ps. The fast Fourier transform (FFT) of the time-resolved magnetization is performed to obtain the simulated FMR spectra [Fig. 2(b)] and space-frequency-resolved 2D profiles (Fig. 3) in order to study the localization of the spin wave modes. The description of the simulations is detailed in Ref. [50]. The simulated dynamic responses are shown in Fig. 2(b) where we observe two resonance peaks for all the ASI configurations at $\phi = 0°$. For $\phi = 45°$, a single peak is observed for SSI while three distinct resonance peaks are seen for each of the KSI and TSI, as shown in Fig. 2(b). The values of the resonance frequencies and the number of modes are in good agreement with the experimental results in Fig. 2(a). The simulated mode profiles are extracted and shown in Fig. 3 for each resonance frequency, identified in Fig. 2(b). For SSI in Fig. 2(b), the resonance modes appear at 9.6 GHz (a_1) and 12.8 GHz (a_2), which are localized in the vertical and the horizontal NMs, respectively, as shown in Fig. 3. The intensity of the spin wave mode becomes higher in the central area of the horizontal nanomagnets owing to the uniform demagnetization along the easy axis. On the other hand, owing to the structural symmetry along 45°, the uniform excitation of spin waves can be observed for all the nanomagnets at $a'_1 = 11.2$ GHz ($\phi = 45°$). According to Fig. 3, the peaks at 10.6 GHz (b_1) and 13 GHz (b_2) for KSI in Fig. 2(b) correspond to the spin wave (SW) modes localized in the tilted and horizontal nanomagnets respectively, as predicted from the experiment using Eq. (3). The intensity of b_1 is larger in Fig. 2(b) owing to the presence of a greater number of tilted NMs compared with the horizontal NMs. Following similar explanation of the
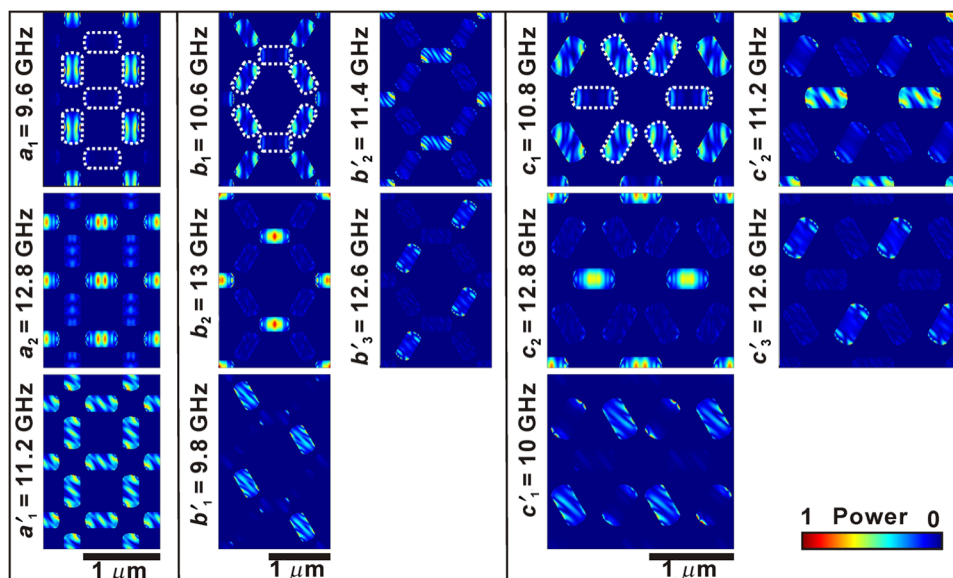

FIG. 3.   Simulated mode profiles at resonance frequencies indicated in Fig. 2(b) for 20-nm-thick Py spin ice structures. The white dotted lines are a guide to the eyes for better understanding of the geometries.

experimental results, three distinct peaks appear at 9.8 GHz (b'_1), 11.4 GHz (b'_2), and 12.6 GHz (b'_3) for KSI at $\phi = 45°$ [Fig. 2(b)], mode profiles (Fig. 3) of which indicate a geometry-selectivity of SW modes in three differently aligned NMs of KSI. Similarly, TSI also exhibits two resonance peaks [Fig. 2(b)] at 10.8 GHz (c_1) and 12.8 GHz (c_2), mode profiles of which indicate the localization of SW modes in tilted and horizontal NMs, respectively (Fig. 3) for $\phi = 0°$. The NM selective response of SW modes can also be observed for $\phi = 45°$ by combining the resonance frequencies at 10 GHz (c'_1), 11.2 GHz (c'_2), and 12.6 GHz (c'_3) in Fig. 2(b) with the corresponding mode profiles shown in Fig. 3. It is worth mentioning that, for the 20-nm-thick Py elements, NM selective responses of SW modes can be obtained with the angular variation of H_{app} for the different lattice arrangements. Thus, these results provide useful insight for potential applications of NM assemblies as microwave filters or on-chip information processing devices through SW. Micromagnetic simulations confirm a similar trend for the variation of resonance frequencies and their space-frequency-resolved SW mode profiles for the 50-nm-thick Py nanostructures at -1.4 kOe (not shown).

We have also studied the effects of film thickness on the dynamic responses of ASI by measuring the FMR spectra while sweeping the field of up to 4.5 kOe at constant frequencies. Shown in Figs. 4(a) and 4(b) are the representative FMR spectra for 50-nm-thick films at $\phi = 0°$ and 45°, respectively, for the three lattice arrangements. For SSI, two fundamental resonance modes of comparable intensities with regular frequency dispersion have been observed, as shown in Fig. 4(a). Following the previous discussions of Fig. 2(a), it can be ascertained that the horizontally aligned NMs contribute to the modes at highest field values and the vertically aligned NMs contribute to the lowest field modes. Interestingly, one extra mode with much lower intensity appears in between the two fundamental modes at the highest and lowest field values. The origin of this mode is probably hybrid in nature and appears owing to the magnetostatic interaction between the NMs. Figure 4(a) shows similar evidence exists for KSI where we observe two fundamental modes at lowest and highest field values, contributed by the tilted and the horizontal NMs, respectively, along with an extra mode in between with much diminished intensity. For TSI in Fig. 4(a), the presence of a shoulder peak is consistently observed with the peak at the highest field. The high-field FMR spectra for 50-nm-thick ASI structures at $\phi = 45°$ are shown in Fig. 4(b). Clear evidence of one fundamental mode exists for the SSI, whereas three fundamental modes are observed for each of KSI and TSI, which is in accordance with the number of modes observed for the 20-nm-thick ASI structures, as shown in Fig. 2(a). The presence of low-intensity hybrid modes is also evident for KSI and TSI at $\phi = 45°$ [Fig. 4(b)]. The field spacing
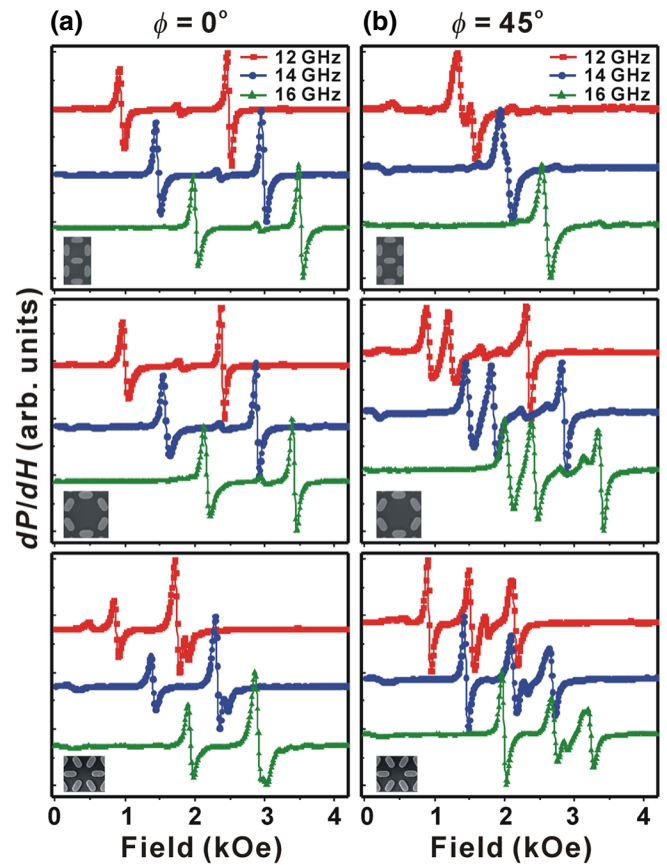

FIG. 4. Experimental FMR spectra at different frequencies for 50-nm-thick Py films with SSI, KSI, and TSI structures (shown as insets) for (a) $\phi = 0°$ and (b) $\phi = 45°$.

between the two fundamental modes is significantly less for TSI compared with that for other lattice arrangements. All the modes show an increase in the resonance fields with the increase in frequency, as shown in Fig. S3 of the Supplemental Material [47]. This directly follows the Kittel equation, as the frequency increases keeping all the demagnetization factors constant, the resonance field as well as the magnetization along the field direction should increase.

The thickness-dependent FMR spectra are shown in Fig. 5(a) for three thicknesses at a fixed h_{rf} frequency of 10.5 GHz for $\phi = 0°$. The resonance fields of the two fundamental modes have been designated by H_1 and H_2, respectively. A marked difference in H_1 and H_2 can be observed as a function of thickness. As H_1 is a low-field mode, each ASI structure manifests a complex state of magnetization, either vortex nucleation, propagation, and annihilation for thicker films or transformation from a single-domain state to uniform magnetization through domain wall motion for the thinner films. In contrast, at higher field values, all the samples are well saturated to a uniformly magnetized state. This difference in the state of magnetization for both the field ranges may be attributed to the observed variation of the two resonance
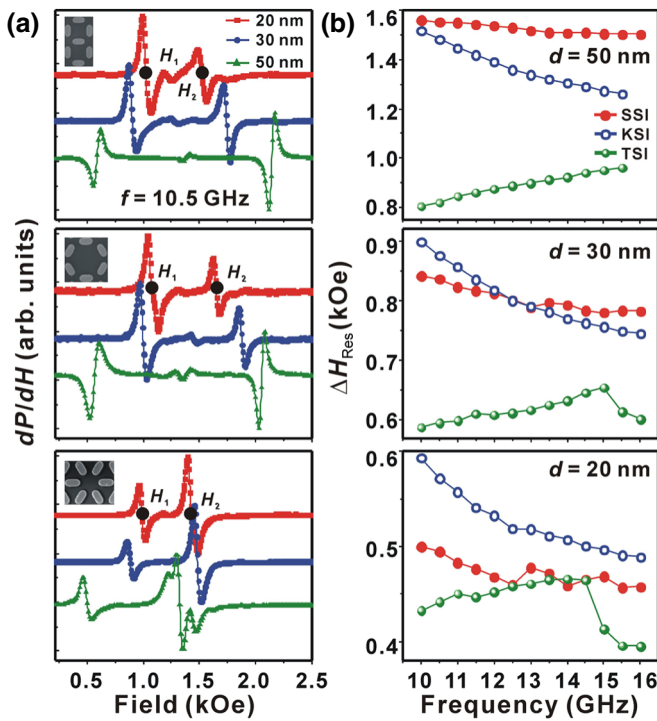
FIG. 5. (a) Thickness-dependent FMR spectra at 10.5 GHz for various spin ice lattice arrangements (shown as insets) for $\phi = 0°$, (b) the frequency dependence of ΔH_{Res} ($H_2 - H_1$) for different ASI geometries of different thicknesses.

fields with thickness. Moreover, the presence of the low-intensity hybrid modes (in between H_1 and H_2) are clearly evident from Fig. 5(a) for 30- and 50-nm-thick ASI structures where the vortex formation takes place [Figs. 1(d) and 1(e)]. The shoulder peak for the TSI has not been observed for the thinner structures at lower frequencies.

We extract the difference of the resonance field values ($\Delta H_{\text{Res}} = H_2 - H_1$) of the fundamental modes at $\phi = 0°$ and plot it as a function of frequency for SSI, KSI, and TSI in Fig. 5(b). We clearly observe that the resonance field difference ΔH_{Res} is markedly sensitive to the lattice arrangements of the spin ice structures and strongly dependent on the film thickness. An almost monotonic decrease in ΔH_{Res} with increasing frequency for the SSI and KSI whereas ΔH_{Res} increases with frequency for the TSI for $d = 50$ nm is observed. Interestingly, for TSI, ΔH_{Res} decreases after 15 and 14.5 GHz for $d = 30$ nm and $d = 20$ nm, respectively. Comparing Fig. 4(a) with Fig. 5(a) for TSI ($\phi = 0°$), we can clearly observe the presence of shoulder mode near the H_2 peak regularly throughout the observed frequency range for 50-nm-thick structures, whereas this shoulder mode is absent for 20- and 30-nm-thick structures. Specifically, the appearance of the shoulder mode has been observed at 15 and 15.5 GHz for the thickness of 20 and 30 nm, respectively (Fig. S4 of the Supplemental Material [47]), which modifies the

field dispersion of H_2 at the specified high-frequency regime and, hence, results in the nonmonotonic variation of ΔH_{Res}. Detailed micromagnetic simulations have been performed in the high-field range 1.5–3 kOe to study the characteristic of FMR spectra for the TSI arrangements where the appearance of extra resonance modes has been observed at the high-field regime for $d = 20$ nm, but a regular frequency dispersion with no extra resonance peaks for $d = 50$ nm (not shown). Thus, our experimental results are strongly complemented by micromagnetic simulations, explaining the role of thickness, lattice arrangement of ASI, and applied field orientations on the static and dynamic properties of ASI.

IV. SUMMARY

In summary, we systematically probe property variations of ASI structures as a function of lattice arrangements of nanomagnets, film thickness and field orientations. The transformation from single-domain nanoelements to complex spin states including vortex is observed with the increase in thickness of the ASI structures. The density of the vortex state and the related magnetization reversal is shown to be markedly sensitive on the ASI geometry and the applied field orientation. Dynamic responses measured with ferromagnetic resonance spectroscopy establish the presence of distinct resonant modes, which are spatially localized in the nanomagnets of different orientations and, hence, can be controlled by the applied field orientations. Understanding of our experimental results is complemented by extensive micromagnetic simulations. Our results explain the potential of spin ice structures in the design of reconfigurable magnonic crystals for microwave filter applications.

[1] R. Jansen, The spin-valve transistor: A review and outlook, J. Phys. D: Appl. Phys. **36**, R289 (2003).

[2] T. R. Albrecht, et al., Bit-patterned magnetic recording: Theory, media fabrication, and recording performance, IEEE Trans. Magn. **51**, 0800342 (2015).

[3] O. Boulle, J. Vogel, H. Yang, S. Pizzini, D. Chaves, A. Locatelli, T. O. Mentes, A. Sala, L. D. Buda-Prejbeanu, O. Klein, M. Belmeguenai, Y. Roussigne, A. Stashkevich, S. M. Chérif, L. Aballe, M. Foerster, M. Chshiev, S. Auffret, I. M. Miron, and G. Gaudin, Room-temperature chiral magnetic skyrmions in ultrathin magnetic nanostructures, Nat. Nanotechnol. **11**, 449 (2016).

[4] A. Talapatra and J. Mohanty, Scalable magnetic skyrmions in nanostructures, Comput. Mater. Sci. **154**, 481 (2018).

[5] J. M. Shaw, S. E. Russek, T. Thomson, M. J. Donahue, B. D. Terris, O. Hellwig, E. Dobisz, and M. L. Schneider, Reversal mechanisms in perpendicularly magnetized nanostructures, Phys. Rev. B **78**, 024414 (2008).

[6] B. Pfau, C. M. Günther, E. Guehrs, T. Hauet, T. Hennen, S. Eisebitt, and O. Hellwig, Influence of stray fields on the switching field distribution for bit-patterned media based on prepatterned substrates, Appl. Phys. Lett. **105**, 132407 (2014).

[7] G. Shimon, A. O. Adeyeye, and C. A. Ross, Magnetic vortex dynamics in thickness-modulated $Ni_{80}Fe_{20}$ disks, Phys. Rev. B **87**, 214422 (2013).

[8] A. De, S. Mondal, C. Banerjee, A. K. Chaurasiya, R. Mandal, Y. Otani, R. K. Mitra, and A. Barman, Investigation of magnetization dynamics in 2D $Ni_{80}Fe_{20}$ diatomic nanodot arrays, J. Phys. D: Appl. Phys. **50**, 385002 (2017).

[9] S. Goolaup, A. O. Adeyeye, and N. Singh, Magnetization reversal mechanisms in diamond-shaped Co nanomagnets, Phys. Rev. B **73**, 104444 (2006).

[10] S. Choudhury, S. Barman, Y. Otani, and A. Barman, Efficient modulation of spin waves in two-dimensional octagonal magnonic crystal, ACS Nano **11**, 8814 (2017).

[11] S. Mallick, S. S. Mishra, and S. Bedanta, Relaxation dynamics in magnetic antidot lattice arrays of Co/Pt with perpendicular anisotropy, Sci. Rep. **8**, 11648 (2018).

[12] S. Choudhury, S. Majumdar, S. Barman, Y. C. Otani, and A. Barman, Active Control of Mode Crossover and Mode Hopping of Spin Waves in a Ferromagnetic Antidot Lattice, Phys. Rev. Appl. **10**, 064044 (2018).

[13] G. Gubbiotti, S. Tacchi, M. Madami, G. Carlotti, Z. Yang, J. Ding, A. O. Adeyeye, and M. Kostylev, Collective spin excitations in bicomponent magnonic crystals consisting of blayer permalloy/Fe nanowires, Phys. Rev. B **93**, 184411 (2016).

[14] J. Ding, M. Kostylev, and A. O. Adeyeye, Magnetic hysteresis of dynamic response of one-dimensional magnonic crystals consisting of homogeneous and alternating width nanowires observed with broadband ferromagnetic resonance, Phys. Rev. B **84**, 054425 (2011).

[15] P. Lupo, Z. Haghshenasfard, M. G. Cottam, and A. O. Adeyeye, Ferromagnetic resonance study of interface coupling for spin waves in narrow NiFe/Ru/NiFe multilayer nanowires, Phys. Rev. B **94**, 214431 (2016).

[16] L. L. Xiong, M. Kostylev, and A. O. Adeyeye, Magnetization dynamics of $Ni_{80}Fe_{20}$ nanowires with continuous width modulation, Phys. Rev. B **95**, 224426 (2017).

[17] L. L. Xiong and A. O. Adeyeye, Dynamic behavior of $Ni_{80}Fe_{20}$ nanowires with controlled periodic width modulation, Appl. Phys. Lett. **108**, 262401 (2016).

[18] G. Gubbiotti, L. L. Xiong, F. Montoncello, and A. O. Adeyeye, Collective spin waves in arrays of permalloy nanowires with single-side periodically modulated width, Appl. Phys. Lett. **111**, 192403 (2017).

[19] M. B. Jungfleisch, J. Sklenar, J. Ding, J. Park, J. E. Pearson, V. Novosad, P. Schiffer, and A. Hoffmann, High-Frequency Dynamics Modulated by Collective Magnetization Reversal in Artificial Spin ice, Phys. Rev. Appl. **8**, 064026 (2017).

[20] L. J. Heyderman and R. L. Stamps, Artificial ferroic systems: Novel functionality from structure, interactions and dynamics, J. Phys.: Condens. Matter **25**, 363201 (2013).

[21] S. Zhang, *Dissertation, Tuning Geometries and Interactions of Artificial Frustrated Nanomagnets* (The Pennsylvania State University, University Park, Pennsylvania, USA, 2013).

[22] R. F. Wang, C. Nisoli, R. S. Freitas, J. Li, W. McConville, B. J. Cooley, M. S. Lund, N. Samarth, C. Leighton, V. H. Crespi, and P. Schiffer, Artificial 'spin ice' in a geometrically frustrated lattice of nanoscale ferromagnetic islands, Nature **439**, 303 (2006).

[23] S. Ladak, D. E. Read, G. K. Perkins, L. F. Cohen, and W. R. Branford, Direct observation of magnetic monopole defects in an artificial spin-ice system, Nat. Phys. **6**, 359 (2010).

[24] Y. Lao, F. Caravelli, M. Sheikh, J. Sklenar, D. Gardeazabal, J. D. Watts, A. M. Albrecht, A. Scholl, K. Dahmen, C. Nisoli, and P. Schiffer, Classical topological order in the kinetics of artificial spin ice, Nat. Phys. **14**, 723 (2018).

[25] I. Gilbert, Y. Lao, I. Carrasquillo, L. O'Brien, J. D. Watts, M. Manno, C. Leighton, A. Scholl, C. Nisoli, and P. Schiffer, Emergent reduced dimensionality by vertex frustration in artificial spin ice, Nat. Phys. **12**, 162 (2016).

[26] J. Sklenar, Y. Lao, A. Albrecht, J. D. Watts, C. Nisoli, G.-W. Chern, and P. Schiffer, Field-induced phase coexistence in an artificial spin ice, Nat. Phys. **15**, 191 (2019).

[27] Z. Budrikis, J. P. Morgan, J. Akerman, A. Stein, P. Politi, S. Langridge, C. H. Marrows, and R. L. Stamps, Disorder Strength and Field-Driven Ground State Domain Formation in Artificial Spin ice: Experiment, Simulation and Theory, Phys. Rev. Lett. **109**, 037203 (2012).

[28] A. Farhan, P. M. Derlet, A. Kleibert, A. Balan, R. V. Chopdekar, M. Wyss, L. Anghinolfi, F. Nolting, and L. J. Heyderman, Exploring hyper-cubic energy landscapes in thermally active finite artificial spin-ice systems, Nat. Phys. **9**, 375 (2013).

[29] A. Farhan, M. Saccone, C. F. Petersen, S. Dhuey, R. V. Chopdekar, Y.-L. Huang, N. Kent, Z. Chen, M. J. Alava, T. Lippert, A. Scholl, and S. van Dijken, Emergent magnetic monopole dynamics in macroscopically degenerate artificial spin ice, Sci. Adv. **5**, eaav6380 (2019).

[30] A. Farhan, A. Scholl, C. F. Petersen, L. Anghinolfi, C. Wuth, S. Dhuey, R. V. Chopdekar, P. Mellado, M. J. Alava, and S. van Dijken, Thermodynamics of emergent magnetic charge screening in artificial spin ice, Nat. Commun. **7**, 12635 (2016).

[31] J. Drisko, T. Marsh, and J. Curnings, Topological frustration of artificial spin ice, Nat. Commun. **8**, 14009 (2017).

[32] T. Dion, D. M. Arroo, K. Yamanoi, T. Kimura, J. C. Gartside, L. F. Cohen, H. Kurebayashi, and W. R. Branford, Tunable magnetization dynamics in artificial spin ice via shape anisotropy modification, Phys. Rev. B **100**, 054433 (2019).

[33] F. Montoncello, L. Giovannini, W. Bang, J. B. Ketterson, M. B. Jungfleisch, A. Hoffmann, B. W. Farmer, and L. E. De Long, Mutual influence between macrospin reversal order and spin-wave dynamics in isolated artificial spin-ice vertices, Phys. Rev. B **97**, 014421 (2018).

[34] W. Bang, M. B. Jungfleisch, F. Montoncello, B. W. Farmer, P. N. Lapa, A. Hoffmann, L. Giovannini, L. E. De Long, and J. B. Ketterson, Coupled macrospins: Mode dynamics

in symmetric and asymmetric vertices, AIP Adv. **8,** 056020 (2018).

[35] M. Saccone, A. Scholl, S. Velten, S. Dhuey, K. Hofhuis, C. Wuth, Y.-L. Huang, Z. Chen, R. V. Chopdekar, and A. Farhan, Towards artificial spin glasses: Thermal ordering in randomized arrays of ising-type nanomagnets, Phys. Rev. B **99,** 224403 (2019).

[36] Y. Li, G. W. Paterson, G. M. Macauley, F. S. Nascimento, C. Ferguson, S. A. Morley, M. C. Rosamond, E. H. Linfield, D. A. MacLaren, R. Maêedo, C. H. Marrows, S. McVitie, and R. L. Stamps, Superferromagnetism and domain-wall topologies in artificial "pinwheel" spin ice, ACS Nano **13,** 2213 (2019).

[37] A. Libál, D. Y. Lee, A. Ortiz-Ambriz, C. Reichhardt, C. J. O. Reichhardt, P. Tierno, and C. Nisoli, Ice rule fragility via topological charge transfer in artificial colloidal ice, Nat. Commun. **9,** 4146 (2018).

[38] X. Zhou, G.-L. Chua, N. Singh, and A. O. Adeyeye, Large area artificial spin ice and anti-spin ice $Ni_{80}Fe_{20}$ structures: Static and dynamic behavior, Adv Funct. Mater. **26,** 1437 (2016).

[39] L. A. S. Mól, A. R. Pereira, and W. A. Moura-Melo, Extending spin ice concepts to another geometry: The artificial triangular spin ice, Phys. Rev. B **85,** 184410 (2012).

[40] M. Donahue, and D. G. Porter, *OOMMF User's Guide, Version 1.0, Intergency Report NISTIR 6376* (National Institute of Standard and Technology, Gaithersburg, MD). http://math.nist.gov/oommf.

[41] A. O. Adeyeye and N. Singh, Large area patterned magnetic nanostructures, J. Phys. D: Appl. Phys. **41,** 153001 (2008).

[42] R. P. Cowburn, Property variation with shape in magnetic nanoelements, J. Phys. D: Appl. Phys. **33,** R1 (2000).

[43] S. Jain, Y. Ren, A. O. Adeyeye, and N. Singh, Configurational anisotropy and control of magnetic vortex chirality in arrays of circular $Ni_{80}Fe_{20}$ nanoscale dots, Phys. Rev. B **80,** 132401 (2009).

[44] M. Jaafar, R. Yanes, A. Asenjo, O. Chubykalo-Fesenko, M. Vázquez, E. M. Gonzalez, and J. L. Vicent, Field induced vortex dynamics in magnetic Ni nanotriangles, Nanotechnology **19,** 285717 (2008).

[45] R. E. Dunin-Borkowski, M. R. McCartney, B. Kardynal, D. J. Smith, and M. R. Scheinfein, Switching asymmetries in closely coupled magnetic nanostructure arrays, Appl. Phys. Lett. **75,** 2641 (1999).

[46] C. I. L. de Araujo, R. C. Silva, I. R. B. Ribeiro, F. S. Nascimento, J. F. Felix, S. O. Ferreira, L. A. S. Mól, W. A. Moura-Melo, and A. R. Pereira, Magnetic vortex crystal formation in the antidot complement of square artificial spin ice, Appl. Phys. Lett. **104,** 092402 (2014).

[47] See Supplemental Material at http://link.aps.org/supplemental/10.1103/PhysRevApplied.13.014034 for hysteresis loops and MFM images for 50-nm-thick ASI at an applied field angle of 45°, simulated hysteresis loops, frequency dependence of resonance field for various modes, and FMR spectra for 20- and 30-nm-thick TSI structure at higher frequencies.

[48] C. Kittel, On the theory of ferromagnetic resonance absorption, Phys. Rev. **73,** 155 (1948).

[49] L. D. Landau and E. Lifshitz, On the theory of the dispersion of magnetic permeability in ferromagnetic bodies, Phys. Z. Sowjetunion **8,** 153 (1935).

[50] D. Kumar and A. O. Adeyeye, Techniques in micromagnetic simulation and analysis, J. Phys. D: Appl. Phys. **50,** 343001 (2017).